

RESEARCH

Open Access



# Macrophage membrane coated nanoscale coordination polymers promote graft survival in allogeneic transplantation

Haili Bao<sup>1,2†</sup>, Shaohua Song<sup>2†</sup>, Hao Liu<sup>2†</sup>, Demei Sun<sup>3</sup>, Xinyuan Zhu<sup>3</sup>, Zhiren Fu<sup>2\*</sup>, Youfu Wang<sup>3\*</sup> and Jinghui Yang<sup>1\*</sup>

## Abstract

Organ transplantation is a crucial life-saving procedure for patients suffering from end-stage organ failure, yet it faces a global shortage. This scarcity not only impacts individual patients but also places strain on healthcare systems worldwide. However, the risk of rejection adds another layer of difficulty to this already intricate medical procedure. Herein, we present the design and synthesis of graft-targeting macrophage membrane coated nanoscale coordination polymers (dNCPs@MM), in which dexamethasone sodium phosphate (DEXp) serves as an effective immunosuppressive drug,  $\text{Fe}^{3+}$  acts as bridging ligands for coordination-driven self-assembly with cargo molecules, and macrophage membranes are utilized to reduce uptake by the immune system as well as a retarder to enhance the blood circulation time. The high drug loading, responsive release behavior and targeting capability of the obtained dNCPs@MM promote their biological performance. In a murine allogeneic heart transplantation model, dNCPs@MM exhibited remarkable efficacy in attenuating acute rejection at a low dosage, with a mean survival time of 14.7 days compared to 8.6 days for DEXp and 9.3 days for dNCPs treatment. At a high dosage, dNCPs@MM exhibited the ability to control established rejection by inducing exhaustion in both  $\text{CD4}^+$  and  $\text{CD8}^+$  T cell and preventing of alloreactive T cells from acquiring effector ( $\text{CD44}^{\text{hi}}\text{CD62L}^-$ ) functions. Moreover, while high doses of DEXp or dNCPs treatment led to significant adverse effects, the administration of dNCPs@MM demonstrates tolerable adverse effects even at high dosage levels. Therefore, dNCPs@MM exhibits promising potential for clinical application in addressing rejections in allografts and xenografts.

<sup>†</sup>Haili Bao, Shaohua Song and Hao Liu contributed equally to this work.

\*Correspondence:

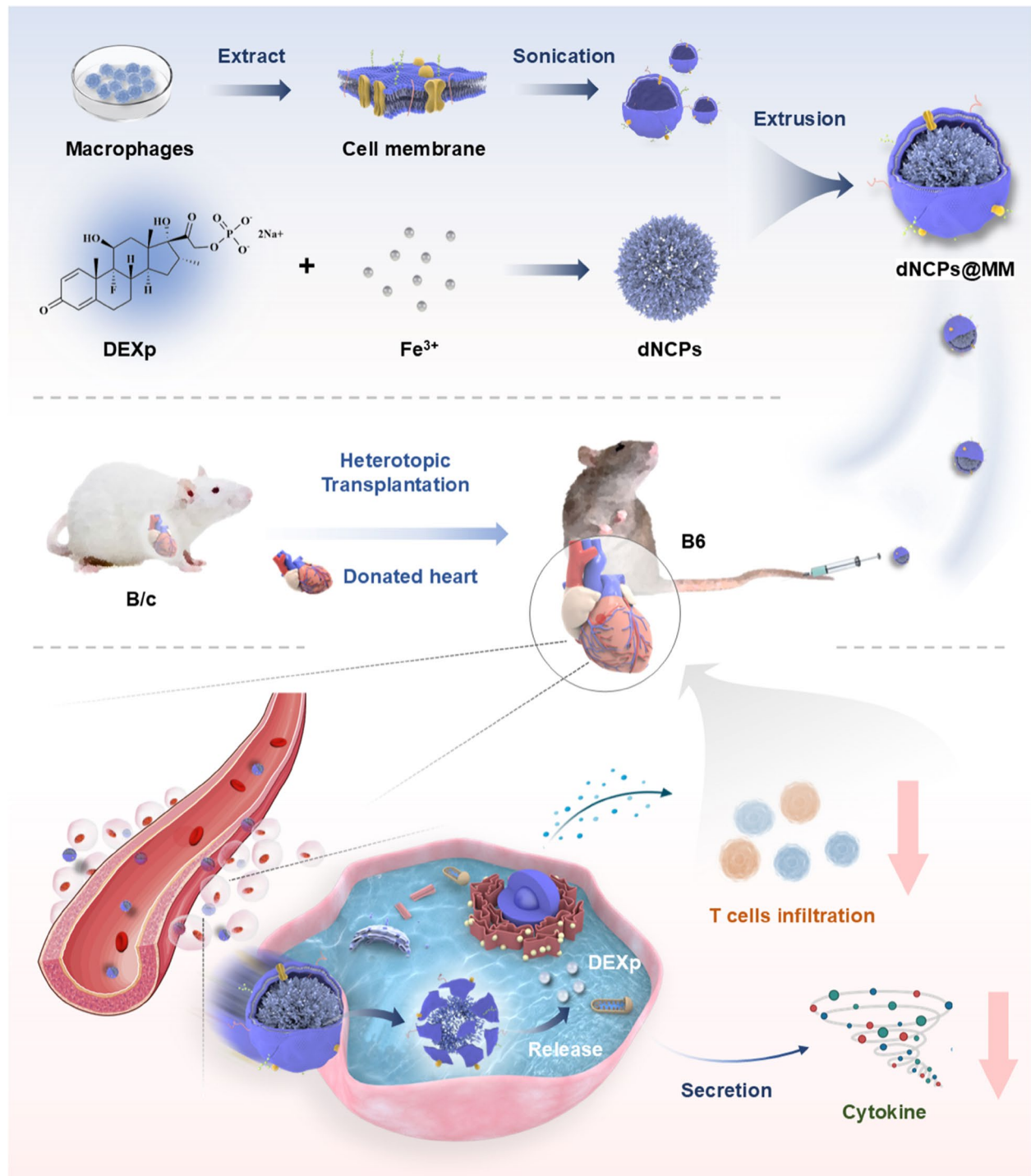
Zhiren Fu  
zhirenf@smmu.edu.cn  
Youfu Wang  
wyfown@sjtu.edu.cn  
Jinghui Yang  
yjhs@smmu.edu.cn

Full list of author information is available at the end of the article



© The Author(s) 2025. **Open Access** This article is licensed under a Creative Commons Attribution-NonCommercial-NoDerivatives 4.0 International License, which permits any non-commercial use, sharing, distribution and reproduction in any medium or format, as long as you give appropriate credit to the original author(s) and the source, provide a link to the Creative Commons licence, and indicate if you modified the licensed material. You do not have permission under this licence to share adapted material derived from this article or parts of it. The images or other third party material in this article are included in the article's Creative Commons licence, unless indicated otherwise in a credit line to the material. If material is not included in the article's Creative Commons licence and your intended use is not permitted by statutory regulation or exceeds the permitted use, you will need to obtain permission directly from the copyright holder. To view a copy of this licence, visit <http://creativecommons.org/licenses/by-nc-nd/4.0/>.

**Graphical Abstract**



**Keywords** Nanoscale coordination polymers, Macrophage membrane, Transplantation, Acute rejection

**Introduction**

Organ transplantation is not only a life-saving procedure for patients with terminal illnesses, but also a complex

and delicate process that necessitates long-term therapeutic intervention. Allogeneic and xenogeneic organ transplantation, despite its benefits, carries the risk of

acute rejection, which is one of the leading causes of graft failure [1, 2]. To mitigate this risk, immunosuppressive agents are used, which have significantly reduced the incidence of acute rejection. Current immunosuppressants have been instrumental in preventing rejection and have demonstrated outstanding anti-rejection effects. However, they also come with a host of off-target adverse effects, including myelosuppression, neuritis, liver damage, and increased risk of cancer, which can be caused by their prolonged usage [3]. Glucocorticoids (GCs) are a class of immunosuppressive drugs that are widely used in clinical settings due to their broad range of physiological activities in inducing and maintaining immunosuppression [4]. They are effective in reducing inflammation and suppressing the immune system, which makes them indispensable in the management of rejection. However, their long-term administration can result in various adverse effects, such as hyperglycemia from islet damage, osteoporosis, and opportunistic infections [5, 6]. To overcome this limitation, it is increasingly imperative to explore innovative strategies for enhancing targeted intravenous delivery. One such approach involves the development of advanced nanoplatforms capable of efficiently delivering GCs directly into rejected grafts, ensuring their effective transportation to the target organs or tissues.

Nanoparticles are extensively researched and utilized in various medical applications, including transplantation, due to their ability to optimize pharmacokinetics and remarkable adaptability [7–10]. In transplantation medicine, nanoparticles offer significant advantages over traditional methods. One of the key challenges in transplantation is achieving effective immunosuppression to prevent organ rejection. Traditional immunosuppressive drugs often exhibit limited efficacy and can cause severe side effects due to their broad systemic distribution. Nanoparticles, however, can be engineered for targeted drug delivery, thereby optimizing pharmacokinetics and minimizing off-target adverse effects [11]. For instance, dexamethasone can be grafted onto macromolecular pre-drugs and forming nanomicelles for passive targeting at inflammatory sites [12]. However, considerations such as poor in vivo stability, inadequate drug loading, and potential kidney risks associated with polymeric materials significantly impact their application. Therefore, A highly efficient nano-drug delivery strategy with active targeting that remains stable in vivo may prove effective for acute rejection treatment.

In doing so, we selected dexamethasone sodium phosphate (DEXp) and designed nanoscale coordination polymers (NCPs) based on DEXp. These nanoparticles consist of DEXp chelated with  $Fe^{3+}$  ions through coordination, exhibiting high drug loading ratio and acid-sensitive release properties for rapid release in acidic

inflammation environments. The selection of  $Fe^{3+}$  ions as bridging ions is based on two key considerations. First, according to the Hard-Soft-Acid-Base principle, hard bases preferentially bind with hard acids, while soft bases have a stronger affinity for soft acids. Phosphoric acid, characterized by its high electronegativity and small size, is classified as a hard base. Conversely, Iron(III) ions ( $Fe^{3+}$ ), as transition metal ions with relatively high charge density, are categorized as hard acids. Consequently, the interaction between  $Fe^{3+}$  and phosphoric acid within the DEXp matrix results in the formation of robust coordination bonds, leading to the creation of stable NCPs. Secondly, compared to other metal ions that can be toxic at higher concentrations and pose risks to cellular health and overall organismal safety,  $Fe^{3+}$  exhibits superior biocompatibility due to its naturally higher physiological concentrations in the human body. However, despite their promising characteristics, these dNCPs suffer from a significant limitation: their insufficient stability in the in vivo environment. To address this limitation, the resulting dNCPs were enveloped with macrophage membranes, thus creating core-shell structured nanoparticles, which we refer to as dNCPs@MM. In this study, we characterized not only the physicochemical properties and in vitro release of dNCPs@MM but also investigated their toxicity, biodistribution, and pharmacokinetics. By employing a murine heterotopic heart transplantation model, we further evaluated the anti-rejection effect of dNCPs@MM, which demonstrated superior immunosuppressive effects and reduced off-target adverse effects. Our study may lay a robust foundation for the clinical feasibility and enhancement of solid organ rejection treatment. The utilization of dNCPs@MM has the potential to improve the treatment by offering a targeted approach to combat rejections in allografts and xenografts.

## Materials and methods

### Preparation of dNCPs

A certain amount of  $FeCl_3 \cdot 6H_2O$  was dissolved in 10 mL of deionized water and then added dropwise to an aqueous solution containing DEXp (51.6 mg, 0.1 mmol) and stirred for 12 h at room temperature. It can be observed that the reaction solution gradually became turbid and light gray. The product was collected by centrifugation at 12,000 rpm for 30 min at 4 °C and washed three times with deionized water. Finally, the prepared metal inorganic drug nanoparticles were lyophilized to obtain dNCPs (yield: 49%).

### Synthesis of Cy3 or Cy5.5 labeled dNCPs

Sulfo-Cyanine3 (Cy3)/ Sulfo-Cyanine5.5 (Cy5.5) (Beyotime, China) was dissolved in deionized aqueous solution containing DEXp avoiding light, followed by the addition of  $FeCl_3$  solution at a 5:1 molar ratio. The mixture was

stirred at room temperature for 12 h in the absence of light. Subsequently, it was purified using a 3500 Da dialysis bag and stored away from light for spare use.

#### Extraction of macrophage membrane

The bone marrow-derived macrophages were extracted from the marrow cavities of femurs and tibias of C57BL/6 mice through flushing with RPMI-1640 containing 10% heat-inactivated Fetal Bovine Serum (FBS). These cells were lysed using RBC lysis buffer and washed in ice-cold tris-magnesium buffer (TM-buffer, pH 7.4, 0.01 M Tris, and 0.001 M MgCl<sub>2</sub>). These cells were cultivated in Petri dishes with high glucose DMEM, 10% FBS, 1% penicillin–streptomycin (P/S), and 20 ng/mL macrophage colony-stimulating factor (Beyotime) to facilitate macrophage differentiation over a 7-day period. Subsequently, the cell suspensions were re-suspended in TM buffer containing 1% protease inhibitor at 4 °C. The cells were ground 50 times with a homogenizer, and centrifugated at 4 °C for 5 min at 3200 rpm. Subsequently, the cells were centrifuged at 4 °C with a rotational speed of 100,000 rpm for 70 min. The supernatant was then discarded, and the precipitate was re-suspended in PBS. Macrophage membrane (MM) vesicles were acquired by repeatedly extruding the suspension through a 0.4 μm polycarbonate porous membrane using an Avanti Mini extruder (repeated 15 times). The MM vesicles were then temporarily stored in PBS solution.

#### Preparation of dNCPs@MM

An aqueous solution containing dNCPs (2 mg) was slowly added to a 200 μL PBS solution containing MM vesicles (extracted from 10<sup>7</sup> cells). Referring to previous research protocols, the mixed solution was first treated in a 100 W ultrasonic shaker for 2 min, followed by extruding the resulting mixture through a polycarbonate porous membrane (pore size: 0.4 μm) 20 times using a Mini extruder. The final product was centrifuged at 15,000 rpm for 30 min at 4 °C to obtain purified dNCPs@MM and washed three times with deionized water. The purified nanoparticles were redispersed in PBS for subsequent experiments.

#### Dynamic Light Scattering (DLS) and Zeta potential

The size and surface charge of dNCPs and dNCPs@MM were recorded on Zetasizer Nano ZS90 (Malvern, England).

#### Transmission electron microscope (TEM)

The size and morphology of dNCPs and dNCPs@MM was evaluated on Tecnai G2 spirit Biotwin (ThermoFisher, America).

#### STEM-EDS-elemental mapping

STEM-EDS mapping was used to confirm the elemental distributionso NCPs using SEM (Hitachi SU-8010) and STEM (FEI Titan G2 80–200).

#### UV-vis

The optical absorbance of related samples was recorded on UV-2600i (Shimadzu, Japan).

#### Thermal gravimetric analysis (TGA) curves of DEXp and dNCPs

TGA was performed using a TG 209 F1 Libra thermos gravimetric analyzer in flowing air atmosphere.

#### SDS-PAGE

Cells and nanoparticles were lysed by RIPA lysis buffer (Beyotime). A BCA kit was then used to assay the protein concentration. The sample was mixed with SDS-PAGE sample loading buffer and heated at 100 °C for 5 min. Samples with the same amount of protein (10 μL/well) were then loaded on an 8% SDS-PAGE gel and electrophoresed for 2 h under constant pressure. The obtained gels were stained with Komas blue for 2 h and analyzed with Quantity One 1-D analysis software (Bio-Rad, Hercules, USA).

#### Western blotting

Cells and nanoparticles were rinsed with PBS twice and lysed in ice-cold RIPA buffer (Beyotime) containing phosphatase and protease inhibitors. Sample proteins were then subjected to 12% sodium dodecyl sulfate-polyacrylamide gel electrophoresis and transferred to nitrocellulose membranes. Membranes were probed with CD11b, F4/80, and CD68 antibodies from Beyotime Biotech. The relative quantity of proteins was determined by a densitometer software (ImageJ, NIH, USA).

#### Release profile of dNCPs and dNCPs@MM

The release profiles of DEXp from dNCPs or dNCPs@MM were studied under various PH environments. dNCPs or dNCPs@MM (10 mg) dispersed in deionized water (4 mL) were put in a dialysis bag (MWCO = 12,000) that was subsequently placed in 35 mL of buffer solution (sitting in a 37 °C shaker with 30× g shaking rate). At various time intervals, 2 mL of incubation media was taken out for HPLC analysis, and 2 mL of medium (fresh) was refilled into the buffer solution.

#### MTT (3-[4,5-dimethylthiazol-2-yl]-2,5 diphenyl tetrazolium bromide) assay

To assess the cytotoxic effect of NPs, a commercial kit (Beyotime, Shanghai) was used to detect the viability of AML-12, RAW264.7, and H9C2 cells. DEXp, dNCPs or dNCPs@MM (0.1–100 μg/ mL, final concentration based

on DEXp) was added in 96-well microplates (9000 cells/well), and then 10  $\mu$ L MTT solution was added. After incubation at 37 °C for 4 h, 100  $\mu$ L Formazan dissolving solution was added individually to each well, and incubated until the purple crystals were completely dissolved. We set the wells with only PBS as the blank group, and the wells with only cells as the control group. The absorbance of each sample was then measured by a microplate reader at a wavelength of 570 nm. The viabilities of AML-12, RAW264.7, and H9C2 cells were determined by comparing with both the blank group and the control group.

#### Intracellular drug release

For intracellular drug release behavior, macrophages were incubated in the media containing at 37 °C for 24 h. the media were replaced with fresh media containing Cy3-dNCPs and Cy3-dNCPs@MM, and the cells were incubated for additional 2, 4, and 6 h, respectively. The results were detected by flow cytometry.

#### Cellular uptake

The cellular uptake were conducted in macrophags. After seeding the cells and incubation at 37 °C for 24 h, the media were replaced with fresh media containing Cy3-dNCPs and Cy3-dNCPs@MM, and the cells were incubated for additional 2, 4, and 6 h, respectively. Subsequently, the cells were washed for three times with PBS buffer and fixed by paraformaldehyde for 15 min. After washing with PBS for three times again, the cells were observed via confocal laser scanning microscopy.

#### Animals

C57BL/6 (B6) mice and BALB/c (B/c)(8–10 weeks old) were purchased from Phenotek Biotechnology (Shanghai, China). All animal experiments were performed in accordance with the guidelines of the National Institute of Health for the Care and Use of Laboratory Animals and approved by the Committee on Ethics of Medicine of Naval Medical University (No. 202403006). The mice were housed in standard animal rooms, and during the post-operative period, the mice were kept in a clean, warm, and quiet environment. All efforts were made to minimize animal suffering and the number of animals used.

#### Heart transplantation

Heterotopic BALB/c hearts were transplanted into the abdomen of C57BL/6 recipients by anastomosing the donor aorta to recipient aorta, and the donor pulmonary artery to the recipient inferior vena cava. The heart grafts were monitored daily until rejection; rejection was defined as complete cessation of pulsation.

#### Assessment of the transplanted heart status

The Stanford Cardiac Surgery Laboratory Graft Scoring System was used for scoring, ranging from 0 (no contraction), 1 (contraction barely visible or palpable), 2 (contraction with a marked decrease in intensity but coordinated contraction nevertheless; disturbed rhythm), 3 (strong, coordinated beats but with a marked decrease in intensity or rate), and 4 (strong contraction of both ventricle at a normal heart rate). Peak aortic velocity (Vp-AO) and posterior left ventricular wall amplitude (A-LVPW) of the transplanted heart were measured using a 10–22 MHz ultrasound probe (Esaote, IT). All analyses were performed by impartial observers.

#### In vivo imaging

To analyze the metabolic characteristic of dNCPs and dNCPs@MM, Cy5.5-dNCPs and Cy5.5-dNCPs@MM dissolved in 100  $\mu$ L PBS was injected into recipients through tail vein. Fluorescence images were captured at 1 h to 24 h post-injection by IVIS Spectrum (PerkinElmer, excitation/emission:675/720, binning = 4, f-stop = 4, exposure time = 1s).

#### Histopathological evaluation

The mice were sacrificed at the indicated time points. The transplanted hearts were cut coronally, fixed in 10% buffered formalin, embedded in paraffin, and sectioned at a thickness of 3  $\mu$ m. The sections were stained with hematoxylin and eosin to assess histological injury. Heart sections were labeled blindly and randomly observed by impartial investigators. The area of myocardial damage was scored according to the percentage of the area of the overall myocardium: 0 (less than 10%), 1 (10–25%), 2 (25–50%), 3 (50–75%), and 4 (75–100%). A semi-quantitative grading system was employed to assess the extent of myocarditis cell infiltration: 0R (no infiltration), 1R (mild infiltration, focal or perivascular), 2R (moderate infiltration, multifocal), and 3R (extensive infiltration, densest and diffuse).

#### Real-time PCR analysis

The total RNA was extracted using TRIzol reagent (Invitrogen, China) according to the manufacturer's instructions. cDNA was transcribed using a Superscript III Reverse Transcriptase Kit (Invitrogen) and oligo d(T) (Applied Biosystems, USA). Quantitative RT-PCR analysis was performed with a SYBR RT-PCR kit (Takara, Japan) and the StepOne Real-Time PCR System (Applied Biosystems). All reactions were conducted in a 20  $\mu$ L reaction volume in triplicate. The relative expression levels for a target gene were normalized against GAPDH.

### Immunofluorescence assay

The paraffin heart sections were de-paraffinized, rehydrated, and handled according to a standard protocol. Then the sections were incubated with CD3, CD4, and CD8 primary antibodies (Beyotime) overnight. After that, the slides were washed three times with PBS and incubated with secondary antibodies for 1 h at room temperature. The nuclei were counter-stained with DAPI. The slides were then observed and imaged using a fluorescent microscope (Nikon 80i, Japan).

### Flow cytometry

Heart grafts, lymph nodes, and splenocytes were collected and prepared for flow cytometry. Dead cells were excluded using Live/Dead solution. An additional dump channel was used to exclude irrelevant cells using a mixture of antibodies (DX5, CD11c, F4/80, and CD19) (Invitrogen). Additional antibodies for CD3, CD4, CD8, CD44, CD62L (Invitrogen) were used to stain T cells. The results were detected by flow cytometry.

### Blood glucose

The mice were sacrificed at the indicated time points. The levels of blood glucose were detected using a glucometer (Roche, Switzerland).

### Serum biochemistry analysis

The mice were sacrificed at the indicated time points. All serum samples were collected and centrifuged at 5000 rpm for 10 min. Creatinine and urea nitrogen were analyzed using an auto-analyzer (Cobas 8000, Roche) with c702 module.

### Statistical analysis

Statistical significance was determined utilizing an ANOVA followed by Bonferroni's test correction using GraphPad Prism 10 (La Jolla, USA). Graft survival curves significance was assessed using a Mantel-Cox log rank test. The results are expressed as the mean  $\pm$  standard deviation (SD). In every case,  $p < 0.05$  was considered statistically significant.

## Results

### Preparation and characterization of dNCPs and dNCPs@MM

Self-assembly strategies driven by the energies of metal-ligand bonding have been demonstrated to be a straightforward and efficient synthetic approach with highly adjustable structural and functional properties. NCPs are commonly defined as assemblies of metal-containing units linked together by organic ligands through coordination interactions with the metal. The utilization of cargoes as organic ligands for assembly can significantly enhance the drug loading capacity and ratio, while also

minimizing potential adverse effects from additional organic ligands. Furthermore, the dosing ratio, loading amount, and loading ratio of the composite drug can be easily adjusted. The nanoscale coordination polymers based on DEXp and iron ions ( $\text{Fe}^{3+}$ ) were synthesized using a "one-step" approach, achieved through coordination-driven self-assembly with cargo molecules serving as bridging ligands. The Dynamic Light Scattering (DLS) results indicated that the average size of dNCPs nanoparticles changes with varying molar ratios of DEXp and  $\text{Fe}^{3+}$  (Fig. 1a). Nanoparticles with a DEXp to  $\text{Fe}^{3+}$  ratio of 5:1 were found to best match our expected particle size ( $< 100$  nm), avoiding being overtaken by the reticuloendothelial system.

In order to enhance the dispersion of nanoparticles and extend their circulation time, dNCPs were further coated with macrophage membranes through co-extrusion using a porous membrane. The results of DLS assay indicated that the average particle size of dNCPs increased from  $(92.2 \pm 8.3$  nm) to  $(107.6 \pm 9.7$  nm) after encapsulation with membranes (Fig. 1b). The zeta potential of dNCPs@MM decreased from  $-27.41$  mV to  $-42.89$  mV upon coating with the macrophage membranes (Fig. 1c). Upon cell membrane encapsulation, a distinct cell membrane shell wrapping around the outer layer of dNCPs was clearly observed, indicating effective coating of dNCPs with macrophage membranes (Fig. 1d, e). UV-vis spectra were further conducted to elucidate the formation and structure of dNCPs. In comparison with free DEXp, dNCPs exhibited a slight redshift at 242 nm, which corresponds to the characteristic absorption peak of DEXp (Fig. 1f). This phenomenon may be attributed to the presence of  $\text{FeCl}_3$  in the nanoparticles. The Fourier transform-infrared spectroscopy (FT-IR) results showed that the phosphate groups in DEXp were involved in the coordination of dNCPs, as indicated by the peaks at  $1101.74$ ,  $991.53$ , and  $891.62$   $\text{cm}^{-1}$  transferring to  $1067.99$  and  $889.68$   $\text{cm}^{-1}$  in the dNCPs (Fig. 1g). X-ray photoelectron spectroscopy (XPS) analysis revealed that the dNCPs spectrum was mainly composed of carbon (C), oxygen (O), Fe, and phosphorus (P) peaks, indicating coordination between DEXp and  $\text{Fe}^{3+}$ . The O 1s binding energy showed a characteristic P-O peak at 532.5 eV. Additionally, the Fe 2p binding energy consisted of a Fe  $2p_{1/2}$  peak at 724.6 eV and a Fe  $2p_{2/3}$  peak at 711.0 eV, confirming the dominance of +3 valence state for Fe in dNCPs (Figure S1). The assembly component and mode were examined using scanning TEM energy-dispersive X-ray spectroscopy (STEM-EDS) analysis, showing the uniform distribution of P and Fe elements in dNCPs (Fig. 1h). To further test the drug loading efficiency of dNCPs, UV-vis was used to detect the absorption values of DEXp and  $\text{FeCl}_3$  at 242 nm and 297 nm, respectively, in order to obtain standard curves (Fig. S2). According

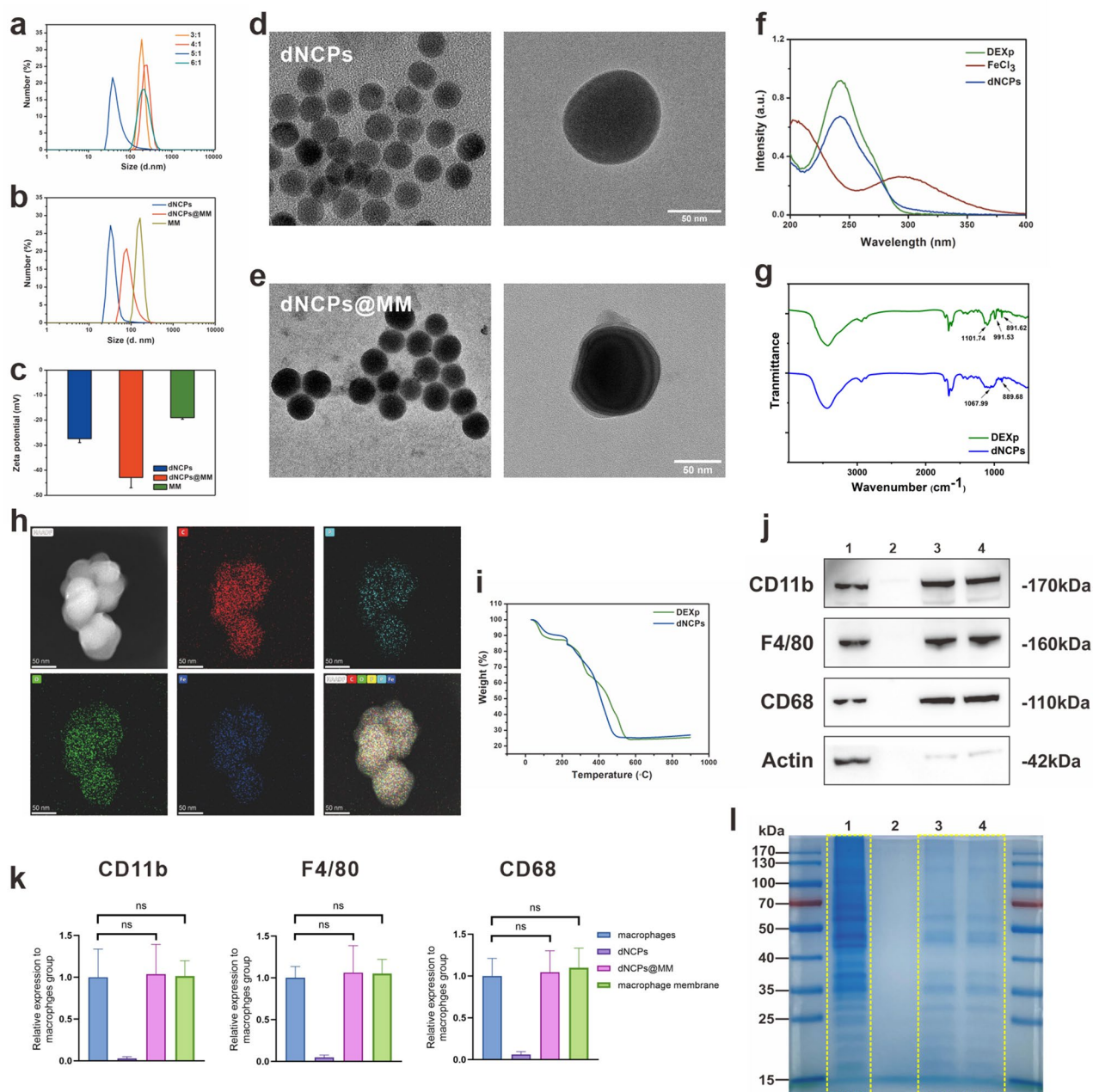


**Fig. 1** Preparation and characterization of dNCPs and dNCPs@MM. **a** Size distributions of dNCPs with different molar ratios of DEXp/Fe<sup>3+</sup> measured by DLS. **b** Size distributions of dNCPs and dNCPs@MM measured by DLS. **c** Zeta potentials of dNCPs and dNCPs@MM. **d** TEM images of dNCPs. Scale bars represent 50 nm. **e** TEM images of dNCPs@MM. Scale bars represent 50 nm. **f** UV-vis spectra of free DEXp, FeCl<sub>3</sub>, and dNCPs in water. **g** Detection of dNCPs and dNCPs@MM by FT-IR spectroscopy. **h** STEM-EDS-elemental mapping of dNCPs, along with the corresponding EDS element maps for red C, green O, indigo P, and blue Fe. Scale bars represent 50 nm. **i** TGA curves of DEXp and dNCPs. **j-k** Western-blot identification of macrophage membrane-associated proteins including CD11b, F4/80, and CD68 (1: macrophages, 2: dNCPs, 3: dNCPs@MM, 4: macrophage membrane). **l** SDS-PAGE protein tracking of retention protein (1: macrophages, 2: dNCPs, 3: dNCPs@MM and 4: macrophage membrane). Data are presented as mean ± s.d. ns *p* > 0.05

to the standard curves, we found that DEXp concentrations were as high as 98.6% before and after dissociation. ICP results indicated that the weight of iron in dNCPs is about 0.78%. TGA results also confirmed that the weight of organic matter is about 99% in dNCPs (Fig. 1i). These results collectively suggested that dNCPs served as an efficient drug loading platform.

Moreover, the nanoparticles were examined through western-blot analysis and sodium dodecyl sulfate polyacrylamide gel electrophoresis (SDS-PAGE). The western-blot analysis unequivocally confirmed the presence of proteins, including CD11b, F4/80, and CD68, on the dNCPs@MM (Fig. 1j, k, Fig. S3). These proteins are known to be crucial for the function and identity of

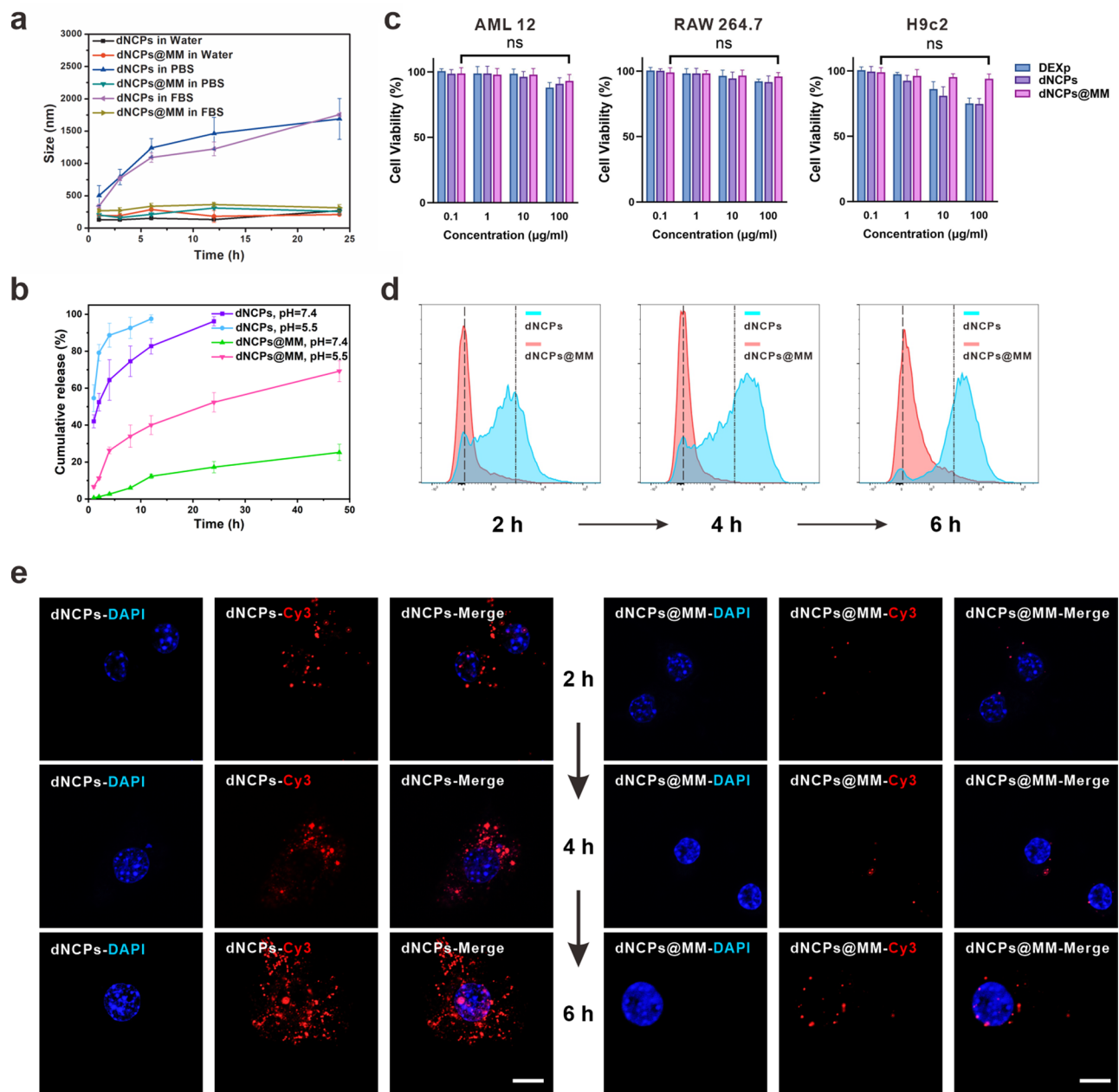


**Fig. 2** Performance analysis of dNCPs and dNCPs@MM in vitro. **a** The stability of dNCPs and dNCPs@MM in various dissolution media. **b** The cumulative release profile of DEXp from dNCPs and dNCPs@MM. **c** Cell viability assays conducted on AML 12, RAW 264.7, and H9c2 cells co-treated with different concentrations (0.1, 1, 10, and 100 µg/mL) of DEXp, dNCPs, and dNCPs@MM respectively. **d** Flow cytometry analysis performed to quantitatively evaluate the uptake of Cy3-labeled dNCPs and Cy3-labeled dNCPs@MM by macrophages. **e** The cellular internalization of Cy3-dNCPs and Cy3-dNCPs@MM by macrophages. Scale bars represent 20 µm. Data are presented as mean ± s.d. ns  $p > 0.05$ , \*\*  $p < 0.01$

macrophages. On the other hand, the SDS-PAGE results revealed that the protein content of dNCPs@MM was virtually identical to those found on the macrophage membrane (Fig. 1l). This finding suggests that the protein composition of dNCPs@MM mirrors that of macrophage membranes, thereby indicating that the cell membrane has been successfully encapsulated on the NPs surface.

**Performance analysis of dNCPs and dNCPs@MM in vitro**

We next evaluated the impact of macrophage membrane coating on enhancing the dispersion and stability of dNCPs nanoparticles. The stabilities of dNCPs and dNCPs@MM in water, PBS buffer solution, and 10% fetal bovine serum (FBS) were assessed using DLS for 24 h. The results indicated that while dNCPs displayed poor stability in PBS and 10% FBS, dNCPs@MM exhibited excellent stability in all three environments. These

core-shell structured nanoparticles demonstrated outstanding *in vitro* stability and could serve as a promising platform for drug delivery (Fig. 2a). We subsequently investigated the influence of pH on the drug release behavior of dNCPs and dNCPs@MM. The results demonstrated that DEXp was rapidly released within a few hours in dNCPs. In stark contrast, only 22.55% of DEXp was released after 48 h of incubation in dNCPs@MM at pH=7.4, while at pH=5.5, the release rate of DEXp significantly increased, exhibiting a burst effect within 8 h, and reached 69.19% after 48 h of co-incubation (Fig. 2b). These findings suggested that the pH-dependent release pattern may be attributed to the acid-triggered dissociation of metal-ligand bonds, and the macrophage membrane-encapsulated dNCPs could maintain stability in complex environments, minimizing premature drug release while rapidly exposing loaded drugs in acidic microenvironments, such as inflamed tissues. To evaluate the biocompatibility of dNCPs@MM, a comprehensive *in vitro* cytotoxicity assessment was conducted. The MTT assay was employed to scrutinize the cytotoxicity of DEXp, dNCPs, and dNCPs@MM on three distinct cell lines, AML 12, H9c2, and RAW 264.7. As expected, negligible cytotoxicity was observed even at a high concentration of 100 µg/ml in dNCPs@MM (Fig. 2c).

Previous research on long-circulating nanoparticles has primarily focused on mitigating their clearance by macrophages [13]. One approach we employed involved coating nanoparticles with macrophage membranes to enhance their immune evasion capability. We examined the cellular uptake efficiency of macrophages in various environments by encapsulating the hydrophilic red fluorescent dye Sulfo-Cyanine3 (Cy3) towards dNCPs and dNCPs@MM to monitor the phagocytic activities. The fluorescence of macrophages incubated with Cy3-dNCPs exhibited a remarkable increase compared to Cy3-dNCPs@MM as the incubation time prolonged (Fig. 2d). To directly investigate macrophage cellular uptake, phagocytosis of nanoparticles by macrophages was observed using confocal fluorescence microscopy (Fig. 2e). Intense red fluorescence was evident after 2 h of incubation of macrophages with Cy3-dNCPs and escalated as incubation progressed, indicating substantial uptake by the macrophages. In contrast, minimal fluorescence was observed in macrophages incubated with Cy3-dNCPs@MM even after 6 h of incubation, suggesting that the membrane-encapsulated drug delivery system may offer an effective strategy to evade macrophage clearance.

#### Graft targeting and anti-rejection capabilities of dNCPs@MM *in vivo*

In order to assess the *in vivo* biological performance of dNCPs@MM, murine allogeneic heart transplantation

was conducted using C57BL/6 recipients of fully MHC mismatched BALB/c heart grafts in this study (Fig. 3a). Recipients treated with saline promptly rejected their allografts, while free DEXp or dNCPs treatment significantly prolonged the survival of allografts after transplantation (mean survival of 8.6 vs. 9.3 days, respectively) (Fig. 3b, c). In contrast, dNCPs@MM greatly promoted graft survival, with a mean survival of 14.7 days. Compared to the DEXp group, the dNCPs group exhibited a higher beating score, although the difference did not reach statistical significance. Notably, dNCPs@MM demonstrated a significant enhancement in beating score compared to other groups (Fig. 3d). Furthermore, the peak aortic velocity (Vp-AO) and the left ventricular posterior wall (A-LVPW) of the heart grafts were measured using Spectral Doppler ultrasound. The quantitative values of Vp-AO and A-LVPW were both significantly higher in the dNCPs@MM group compared to the other groups, indicating a superior preservation of heart graft function (Fig. 3e, f).

After the intravenous administration of Cy5.5, Cy5.5-dNCPs, and Cy5.5-dNCPs@MM, fluorescence images of mice were acquired using a small animal fluorescence imaging system at 1, 2, 4, 8, 12, and 24 h post-injection. The results demonstrated that, in comparison with the Cy5.5-dNCPs group and the free Cy5.5 group, the circulation time of Cy5.5-dNCPs@MM group was significantly prolonged. Furthermore, a more pronounced accumulation of fluorescent substances was observed at the transplanted heart sites in the abdomen of mice treated with Cy5.5-dNCPs@MM (Fig. 3g). Moreover, the resected major organs (including heart, liver, spleen, lung, kidney) and plasma were examined using a fluorescence imaging system 24 h after injection. In addition to the livers and grafts, a significant increase in fluorescence intensity was also observed in the plasma (Fig. 3h). These findings suggest that dNCPs@MM not only have the ability to accumulate in allografts but also exhibit prolonged blood circulation duration.

#### The dNCPs@MM treatment attenuated rejection-induced graft injury and diminished lymphocyte infiltration

The histological evidence was further obtained by hematoxylin and eosin (H&E) staining (Fig. 4a). While the free DEXp and dNCPs groups exhibited a certain protective effect compared to the saline group, there was still noticeable lymphocyte infiltration, cardiomyocyte necrosis, and congestion in grafts. Conversely, grafts from mice treated with dNCPs@MM exhibited minimal loss of integrity and barely noticeable congestion, resulting in lower injury and inflammatory cell infiltration scores (Fig. 4b, c). Given that cytokines secreted by various immune cells, including T lymphocytes, play a crucial role in the pathogenesis of rejection, we conducted a

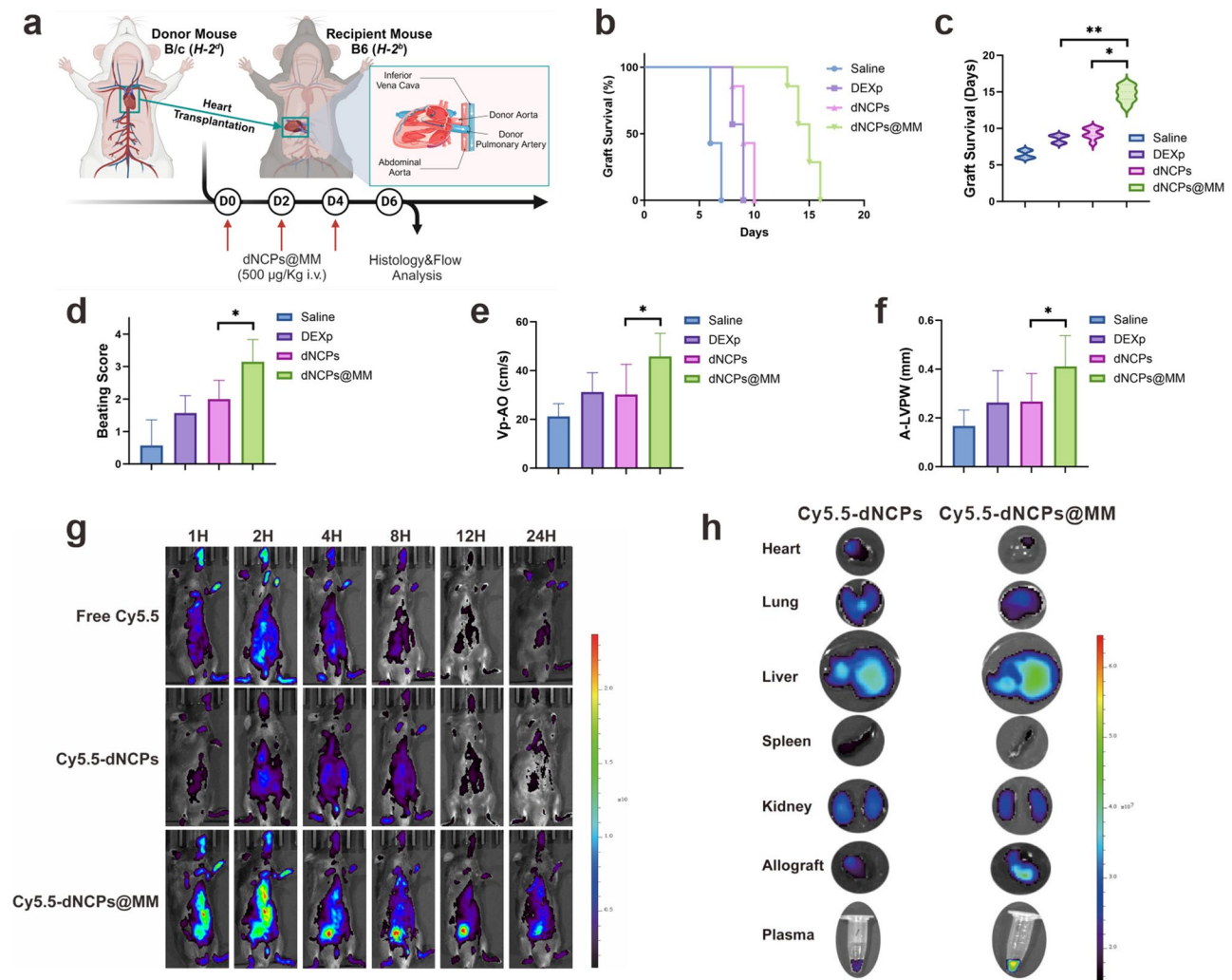


**Fig. 3** Graft targeting and anti-rejection capabilities of dNCPs@MM in vivo. **a** Experimental schedule for the treatment of transplanted mice with dNCPs@MM. The figure was created with BioRender.com. **b** Survival curves of the cardiac allografts in mice. **c** Survival days of the cardiac allografts in mice. **d** Heart beating score assessed by The Stanford Cardiac Surgery Laboratory Graft Scoring System. **e** Peak aortic velocity (Vp-AO) and **f** Posterior left ventricular wall amplitude (A-LVPW) of the transplanted heart measured by ultrasound imaging. **g** Real-time in vivo NIR imaging of mice with cardiac allograft following administration of free Cy5.5, Cy5.5-dNCPs, or Cy5.5-dNCPs@MM. **h** Ex vivo imaging of resected organs and plasma at 24 h post-injection. Data are presented as mean  $\pm$  s.d. \*  $p < 0.05$ , \*\*  $p < 0.01$

comparison of cytokine expression levels (TNF- $\alpha$ , IFN- $\gamma$ , IL-1 $\beta$ , IL-2, and IL-6) among different groups (Fig. 4d). The results revealed a significant reduction in the secretion of TNF- $\alpha$ , IFN- $\gamma$ , IL-1 $\beta$ , IL-2, and IL-6 in the other three groups (DEXp, dNCPs and dNCPs@MM) compared to the saline group, with notably superior performance observed in the dNCPs@MM group. Considering that the recruitment and infiltration of T lymphocytes into grafts are the primary drivers of cellular rejection, we next assessed CD3 through immunofluorescence 6 days post transplantation (Fig. 4e, f). The results revealed a significant reduction in the quantity of CD3<sup>+</sup> cells in the dNCPs@MM group compared to the other groups, indicating effective inhibition of bulk T cell infiltration by dNCPs@MM. Moreover, dNCPs@MM treatment led to a

uniform reduction of T lymphocyte subsets identified by immunofluorescence targeting CD4 and CD8 in grafts, demonstrating its broad inhibitory capacity against T lymphocytes (Fig. 4g, h).

**The dNCPs@MM treatment resulted in a reduction of graft-infiltrating T cells and a shift in their effector phenotypes**  
 Previously, we have reported that graft-infiltrating T cells are more likely to be donor specific and can rapidly elaborate effector function [14–16]. In order to gain a deeper insight into the impact of dNCPs@MM on graft-infiltrating T cells, we grafted the fully MHC mismatched BALB/c heart allografts into C57BL/6 and compared the profiles of graft-infiltrating CD4<sup>+</sup> and CD8<sup>+</sup> T cells at the peak of the rejection response (day 6) (Fig. 5a, b). Flow

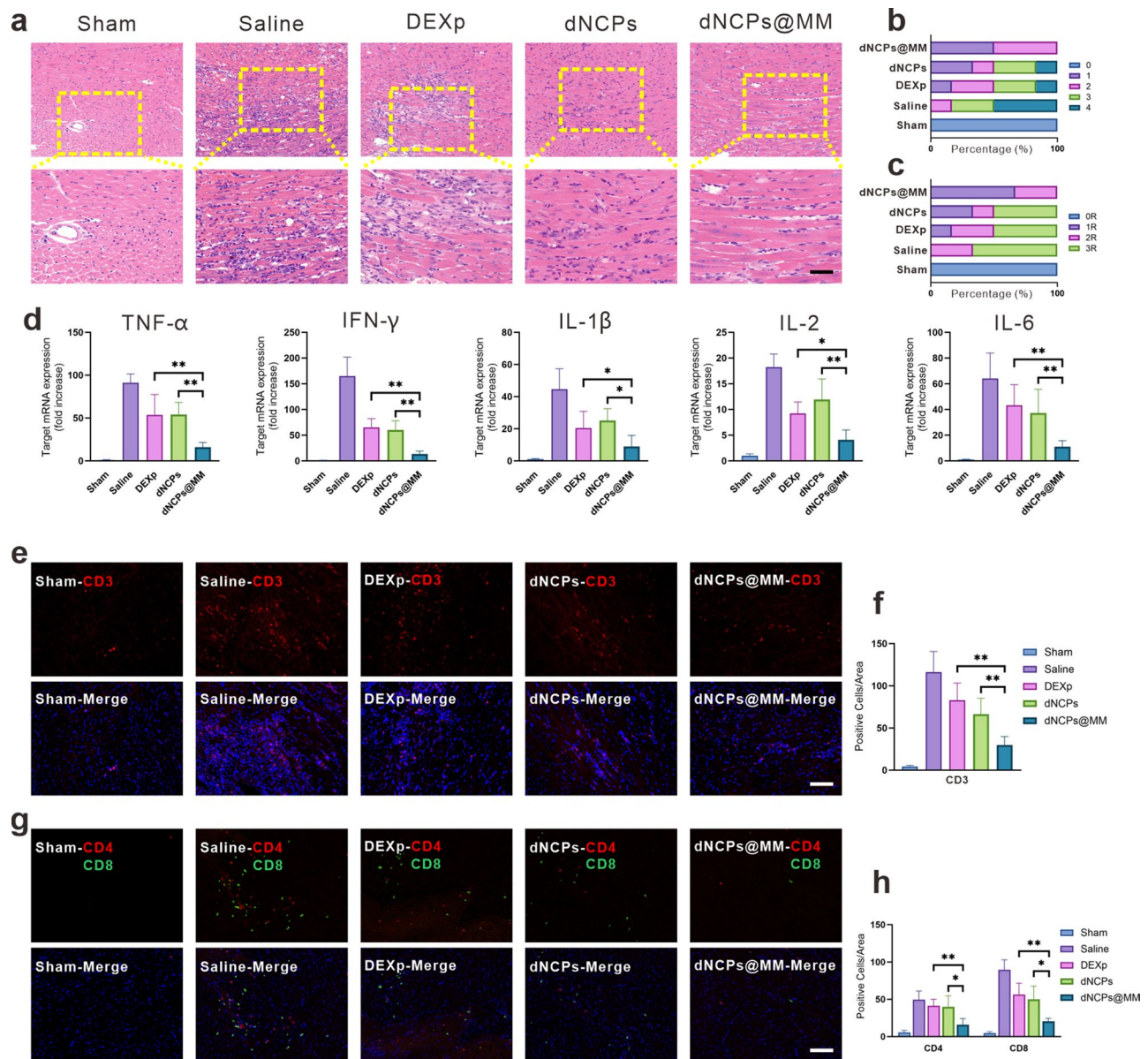


**Fig. 4** In vivo graft protective effects of dNCPs@MM through its anti-rejection and anti-inflammatory properties. **a** Representative H&E staining of the grafts 6 days post transplantation. Scale bars represent 50  $\mu$ m. **b** The myocardial injury of the grafts assessed using a semi-quantitative grading method 6 days post transplantation. **c** The degree of inflammatory cell infiltration evaluated by semi-quantitative grading 6 days post transplantation. **d** The mRNA levels of TNF- $\alpha$ , IFN- $\gamma$ , IL-1 $\beta$ , IL-2, and IL-6 in graft tissues. **e** Representative fluorescence images of graft sections stained with CD3 and DAPI. Scale bars represent 50  $\mu$ m. **f** The count of the CD3<sup>+</sup> cells. **g** Representative fluorescence images of graft sections stained with CD4, CD8, and DAPI. Scale bars represent 50  $\mu$ m. **h** The count of the CD4<sup>+</sup> and CD8<sup>+</sup> cells. Data are presented as mean  $\pm$  s.d. \*  $p < 0.05$ , \*\*  $p < 0.01$

cytometry analysis revealed a substantial retrieval of graft-infiltrating T cells from the transplanted heart following treatment with DEXp or dNCPs, and the overall population of CD4<sup>+</sup> and CD8<sup>+</sup> T cells was further significantly reduced with dNCPs@MM treatment (Fig. 5c). Moreover, analysis of the CD4<sup>+</sup> and CD8<sup>+</sup> compartments, based on CD44 and CD62L expression, yielded similar profiles in both DEXp and dNCPs groups. In contrast, a notable difference was observed in the dNCPs@MM group, where both CD4<sup>+</sup> and CD8<sup>+</sup> subsets exhibited a

predominantly CD44 phenotype and largely downregulated the expression of CD62L, consistent with an effector phenotype.

We also conducted an analysis of the T cells in the secondary lymphoid organs of the host 6 days post-transplantation. The total number of CD4<sup>+</sup> and CD8<sup>+</sup> T cells, as well as the percentages of CD44<sup>hi</sup>CD62L<sup>-</sup> effector T cells within both CD4<sup>+</sup> and CD8<sup>+</sup> subsets, exhibited consistent reductions in the dNCPs@MM group compared to other groups in draining lymph nodes. To our surprise,

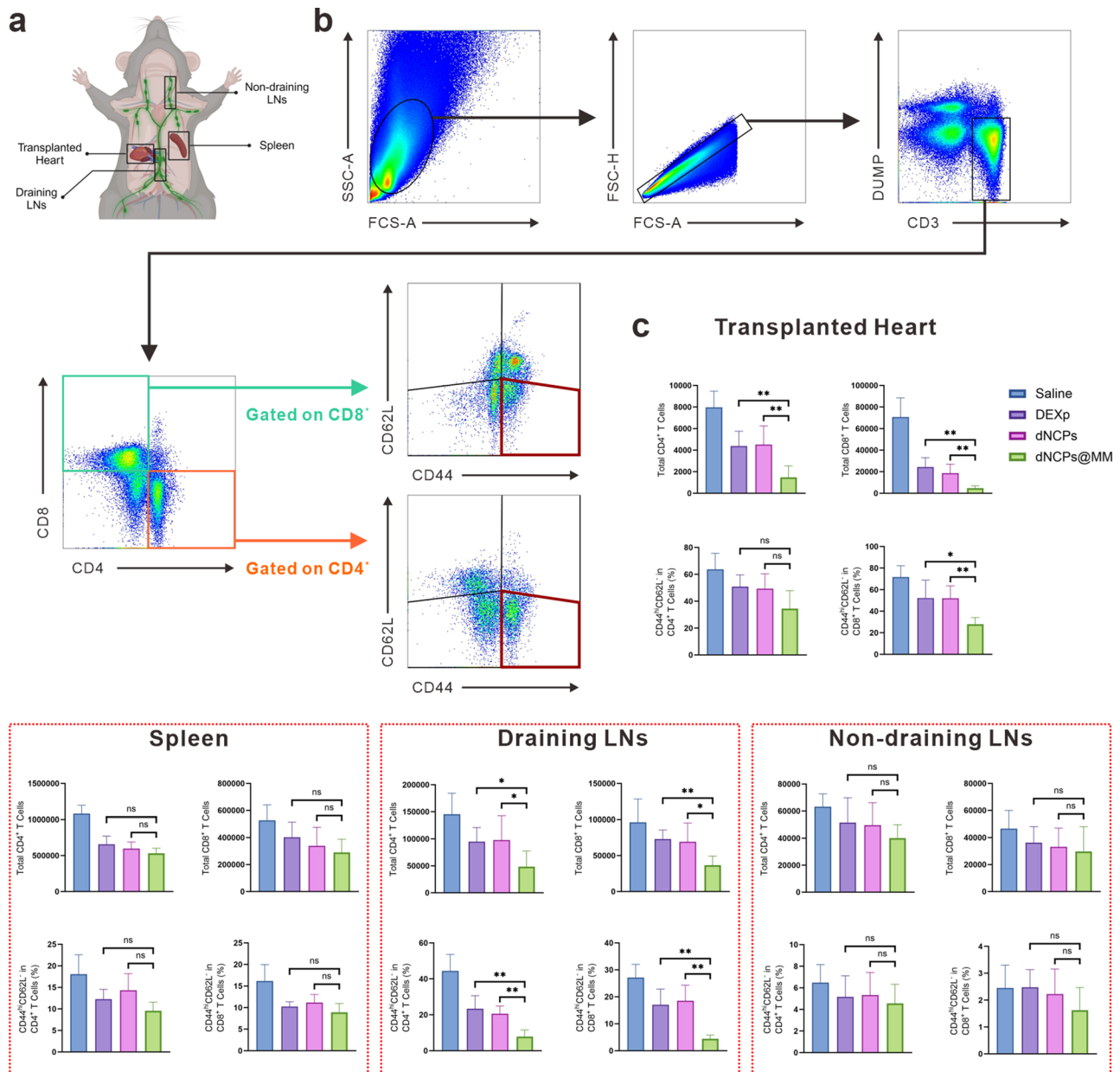


**Fig. 5** The diminished graft-infiltrating T cells displayed compromised effector phenotypes following dNCPs@MM treatment. **a** Schematic representation of harvested organs and lymph nodes. The figure was created with BioRender.com. **b** Gating strategy and representative FACS plots of graft-infiltrating T cells. **c** The numbers of graft-infiltrating T cells and the percentages of CD44<sup>hi</sup>CD62L<sup>-</sup> among CD4<sup>+</sup> or CD8<sup>+</sup> T cells in transplanted heart, spleen, draining lymph nodes, and non-draining lymph nodes. Data are presented as mean ± s.d. ns *p* > 0.05, \* *p* < 0.05, \*\* *p* < 0.01

both CD4<sup>+</sup> and CD8<sup>+</sup> subsets were found to be similar across all four groups, either in absolute cell numbers or at a relative percentage of CD44<sup>hi</sup>CD62L<sup>-</sup> effector T cells in spleen and non-draining lymph nodes.

**Successful rescue of rejected grafts with delayed high-dose dNCPs@MM treatment**

To mimic the clinical transplantation scenario in which rejection is often detected several days after its initiation, we characterized the impact of delayed high-dose

dNCPs@MM treatment on ongoing T cell-mediated acute rejection (Fig. 6a). The allografts in the DEXp and dNCPs groups exhibited a high rate of failure on day 13–14, whereas the dNCPs@MM treatment significantly promoted graft survival, with an average survival period of 18.57 days (Fig. 6b, c). Histologic examination of day 10 allografts from both the high-dose DEXp and dNCPs groups revealed a significantly higher degree of tissue damage and cellular infiltration compared to the high-dose dNCPs@MM treatment, leading to increased

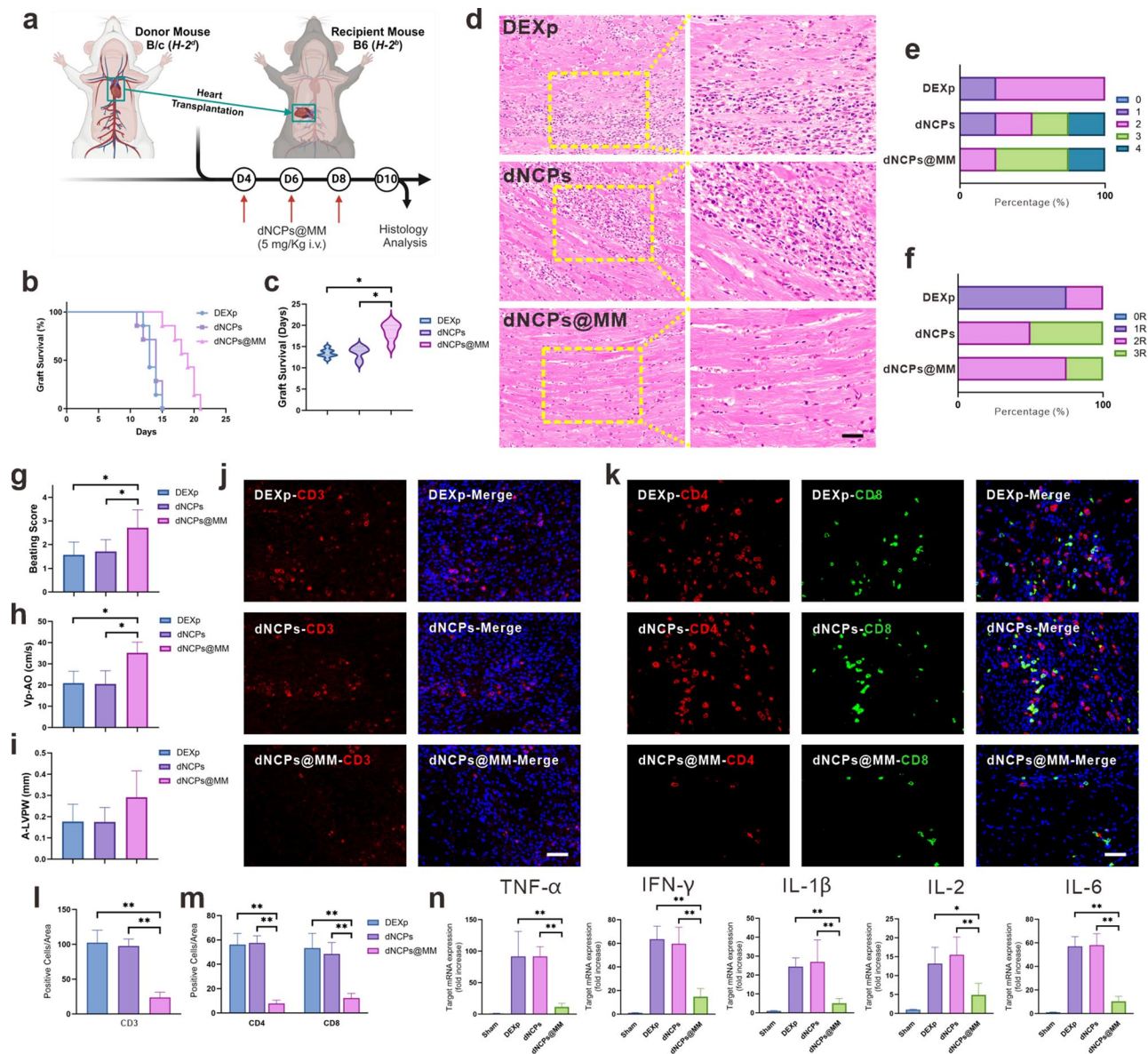


**Fig. 6** Delayed dNCPs@MM treatment was able to halt ongoing T-cell-mediated acute rejection. **a** Experimental schedule for the treatment of transplanted mice with dNCPs@MM. The figure was created with BioRender.com. **b** Survival curves of the cardiac allografts in mice. **c** Survival days of the cardiac allografts in mice. **d** Representative H&E staining of the grafts 10 days post transplantation. Scale bars represent 50  $\mu$ m. **e** The myocardial injury of the grafts assessed using a semi-quantitative grading method 10 days post transplantation. **f** The degree of inflammatory cell infiltration evaluated by semi-quantitative grading 10 days post transplantation. **g** Heart beating score assessed by the Stanford Cardiac Surgery Laboratory Graft Scoring System. **h** Peak aortic velocity (Vp-AO) and **i** Posterior left ventricular wall amplitude (A-LVPW) of the transplanted heart measured by ultrasound imaging. **j** Representative fluorescence images of graft sections stained with CD3 and DAPI. Scale bars represent 50  $\mu$ m. **k** Representative fluorescence images of graft sections stained with CD4, CD8, and DAPI. Scale bars represent 50  $\mu$ m. **l** The count of the CD3<sup>+</sup> cells. **m** The count of the CD4<sup>+</sup> and CD8<sup>+</sup> cells. **n** The mRNA levels of TNF- $\alpha$ , IFN- $\gamma$ , IL-1 $\beta$ , IL-2, and IL-6 in graft tissues. Data are presented as mean  $\pm$  s.d. \*  $p < 0.05$ , \*\*  $p < 0.01$

injury and inflammatory cell infiltration scores (Fig. 6d-f). The other semi-quantitative gradings, including the heart beating score, Vp-AO, and A-LVPW, also exhibited a similar trend among the groups, albeit all groups experienced a decrease in scores compared with treatment from the start of transplantation (Fig. 6g-i). Quantification of the total numbers of graft-infiltrating CD3<sup>+</sup> T cells at day 10 post-transplantation revealed a 4.31-fold

increase in DEXp-treated recipients and a 4.11-fold increase in dNCPs treated recipients, compared to grafts from dNCPs@MM recipients (Fig. 6j, l). These findings were confirmed with immunofluorescence of graft-infiltrating CD4<sup>+</sup> and CD8<sup>+</sup> T cells, where reduced cellular infiltrate was observed in allografts receiving dNCPs@MM compared to those receiving DEXp or dNCPs (Fig. 6k, m). Furthermore, the decreased infiltration of T

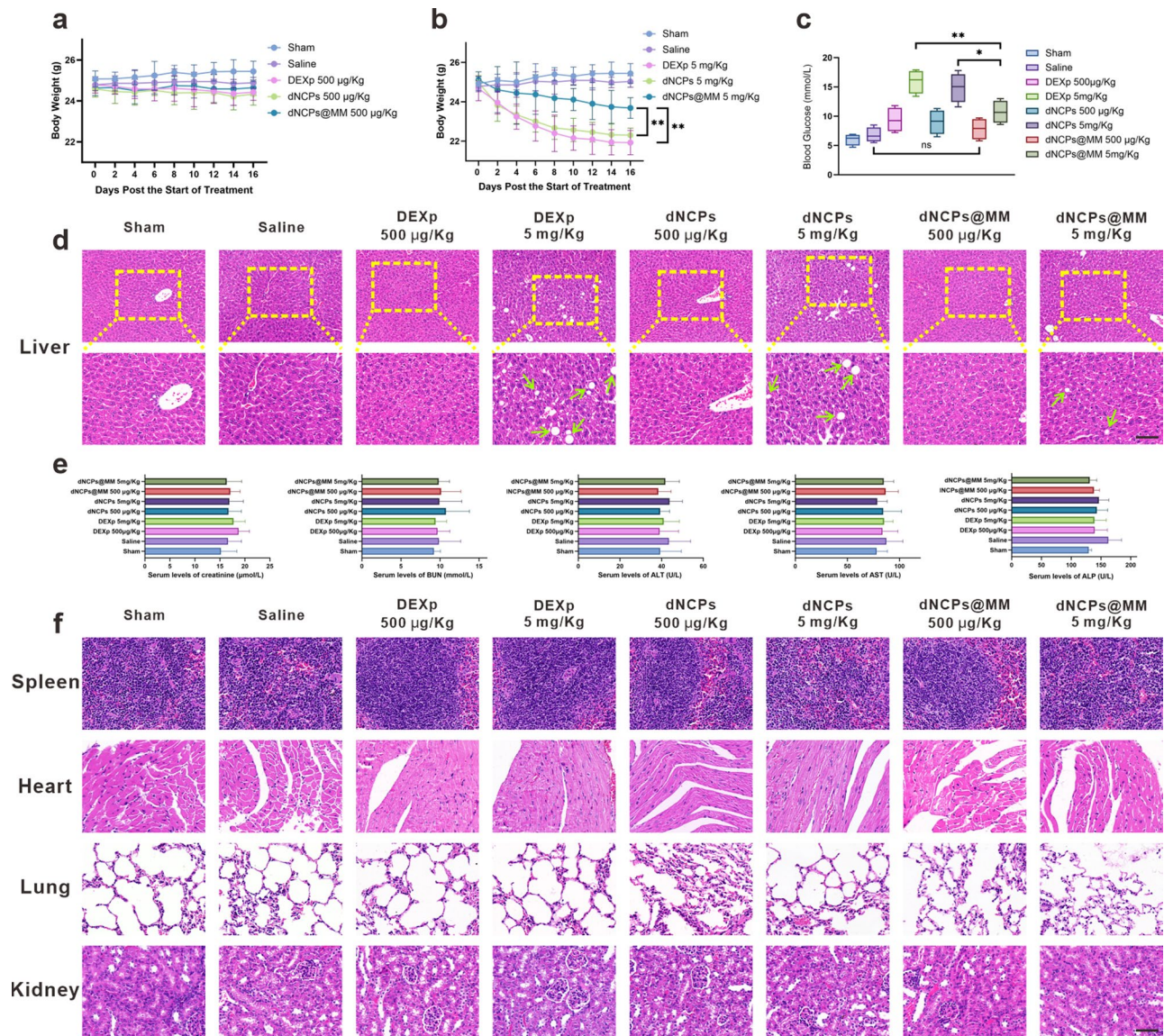


**Fig. 7** dNCPs@MM exhibited reduced adverse effects and exceptional biocompatibility. **a** Variations in body weights of mice following low-dose treatments. **b** Variations in body weights of mice following high-dose treatments. **c** Alterations in blood glucose levels of mice following various treatments. **d** Representative H&E staining of the recipient liver. Green Arrowheads indicate lipid droplets. Scale bars represent 100 µm. **e** Serum level of creatinine, urea nitrogen (BUN), alanine aminotransferase (ALT), aspartate aminotransferase (AST), and alkaliphosphatase (ALP). **f** Representative H&E staining of recipient major organs including kidney, heart, lung, and spleen. Scale bars represent 100 µm. Data are presented as mean ± s.d. ns  $p > 0.05$ , \*  $p < 0.05$ , \*\*  $p < 0.01$

cells into the graft also led to a reduction in proinflammatory cytokines in allografts that received dNCPs@MM compared to those that received DEXp or dNCPs (Fig. 6n).

**dNCPs@MM demonstrated reduced adverse effects and exceptional biocompatibility**

GCs constitute the most important and frequently used class of immunosuppressive drugs due to their potent anti-rejection capability. However, there is also a counterbalancing perspective on GCs, stemming from concerns about their systemic adverse effects resulting from

cumulative exposure, thereby impeding their utilization [17]. In this study, we observed that recipient mice treated with high doses of DEXp or dNCPs experienced a reduction in body weight compared to those treated with dNCPs@MM, while no significant changes were noted following the low-dose treatment (Fig. 7a, b). On the day of sacrifice, the blood glucose levels of mice were evaluated. Importantly, high doses of DEXp or dNCPs led to a marked elevation in blood glucose levels in the recipient mice. In contrast, the blood glucose levels of mice treated with high doses of dNCPs@MM showed a slight increase compared to the control group and were comparable to

those observed with low doses of DEXp or dNCPs treatment (Fig. 7c). We subsequently investigated the adverse effects on major organs of the recipients. Histological examination revealed a sizable accumulation of lipid droplets in the livers of high -dose DEXp- or dNCPs-treated recipients, whereas high -dose dNCPs@MM treatment resulted in only minimal lipid droplet formation (Fig. 7d). Taken together, our data indicate that the administration of dNCPs@MM demonstrates tolerable adverse effects even at high dosage levels.

Unlike the significant adverse effect of GCs on liver, histological analysis of other recipient major organs revealed no evidence of toxicity even at high treatment doses in all groups (Fig. 7f). Moreover, the hemolytic assay demonstrated that the dNCPs@MM did not induce significant hemolysis, indicating its excellent hemocompatibility (Fig. S4). These observations were further supported by the results of comprehensive blood biochemistry analysis in recipient following dNCPs@MM treatment, revealing favorable tolerability at the administered dose (Fig. 7e).

## Discussion

Organ transplantation is a critical life-saving procedure for patients suffering from end-stage organ failure. However, the global shortage of suitable donor organs presents a significant challenge [18]. Addressing this issue by exploring alternative sources of organs for transplantation has become an urgent priority in healthcare. Xenotransplantation, involving genetically engineered organs or tissues from different species, has emerged as a promising solution to this dilemma. Notably, following the world's first pig-to-human kidney xenotransplantation into brain-dead decedents in 2021, clinical exploration of xenotransplantation has experienced rapid growth in recent times. Despite efforts having been made to utilize CRISPR–Cas9 technology for the design and engineering of humanized porcine donors, the long-term survival of xenografts still faces huge challenges due to persistent xenogeneic immunologic barriers [19]. Recently, a study of scRNA-seq on two instances of pig-to-human kidney xenotransplantation revealed substantial peripheral immune activation and infiltration of human immune cells into porcine xenografts [20]. In light of this, it is recommended to consider strategies such as employing higher doses and more potent immunosuppressive drugs to address this challenge; however, these approaches may be accompanied by significant systemic adverse effects. These concerns prompt us to explore nanotechnology-based targeted immunosuppression with minimal adverse effects in addressing this challenge. Recent advancements in nanomaterial design have witnessed a significant paradigm shift towards developing more biocompatible and long-circulating membrane-based delivery nanosystems [21]. These systems effectively mimic

the biological features of their source cells while retaining the essential physicochemical properties of nanoparticles. The membrane cloaking technique preserves the intact proteolipid composition and the complex set of surface proteins, which are crucial for effective biointerfacing. By leveraging the unique properties of cell membranes, particularly those of macrophages, researchers can develop sophisticated nanocarriers that offer enhanced biocompatibility, prolonged circulation, and precise targeting capabilities [22, 23].

In this article, we present the design and synthesis of graft-targeting dNCPs@MM, in which DEXp serves as an effective immunosuppressive drug,  $\text{Fe}^{3+}$  acts as bridging ligands for coordination-driven self-assembly with cargo molecules, and macrophage membranes are utilized to escape immune recognition as well as a retarder to enhance the blood circulation time of the dNCPs@MM. The resulting NPs have been successfully used for targeted immunosuppression in a fully MHC-mismatched murine heterotopic heart transplantation model ( $H-2^d$  to  $H-2^b$ ). While the utilization of whole cells as carriers has been explored, current research in this area has predominantly focused on cell membrane coatings for surface functionalization of NP cores [24, 25]. Through the application of a thin layer of natural macrophage cell membrane enveloping an inner core of dNCPs, we have successfully generated a more biocompatible and long-circulating nanopatform. This approach to membrane cloaking preserves the intact proteolipid composition and the complex array of surface proteins essential for effective biointerfacing, thereby imparting dNCPs@MM with the desirable immunogenicity characteristic of the parent cells. The present research explains the prolonged blood circulation of dNCPs@MM is a consequence of the protection of outer layer of macrophage membrane on inner metal-ligand bonds and the efficient evasion of macrophage clearance, as manifested by in vitro drug release assays and macrophage uptake experiments.

The current immunosuppressive regimens in solid organ transplantation heavily rely on GCs due to the unique and multifaceted molecular mechanisms of GCs [26]. The immunosuppressive mechanisms induced by GCs encompass: inhibition of IL-2 to deplete T cells, thereby preventing Th1 differentiation and leading to T cell apoptosis; suppression of B cell clonal expansion by inhibiting the production of IL-2 and related peptides, resulting in reduced antibody production; direct or IL-5-mediated induction of eosinophil apoptosis; downregulation of Fc receptors and MHC class II molecules on macrophage surface through inhibition of proinflammatory cytokines; acceleration of lymphocyte apoptosis and abrogation of alloimmune responses to third-party antigens [27–30]. These mechanisms are consistent with our previous finding that a single 200  $\mu\text{g}$  bolus dose of GCs

(methylprednisone) remained significant in its impact [31]. With the certified excellent stability and biocompatibility of dNCPs@MM demonstrated in vitro, we utilized a murine heart transplantation model in this study to investigate the impact of dNCPs@MM on allografts and graft-infiltrating T cells. In the absence of intervention, allogeneic hearts completely stopped beating on day 7 post-transplantation, whereas low-dose (500 µg/Kg) administration of dNCPs@MM effectively halted the rejection process and extended graft survival by an additional 7 days. This dosage represents approximately one-tenth of the dexamethasone dosage used in previous studies [32, 33]. The primary mechanism underlying graft acceptance appears to involve the induction of both CD4<sup>+</sup> and CD8<sup>+</sup> T cell exhaustion, as well as the inability of alloreactive T cells to acquire effector (CD44<sup>hi</sup>CD62L<sup>-</sup>) functions.

Previous studies have indicated that the use of GCs alone is associated with a certain percentage of failure in halting ongoing allograft rejection [34–36]. To address this concern, we allowed alloreactive immune cells to develop responses against fully MHC-mismatched heart transplantation 4 days prior to initiating high-dose (5 mg/Kg) dNCPs@MM treatment, when there were already significant, if not peak levels of primed CD4<sup>+</sup> and CD8<sup>+</sup> T cells infiltration into the allograft. Importantly, delayed administration of high-dose dNCPs@MM treatment effectively enhanced graft survival and inhibited the accumulation of both CD4<sup>+</sup> and CD8<sup>+</sup> T cells in the allograft, thus confirming that its efficacy extends beyond mere inhibition of de novo rejection.

While dNCPs@MM have shown remarkable efficiency in directly delivering GCs to rejected grafts, thereby enhancing therapeutic efficacy, the long-term administration of relatively high doses of GCs raises valid concerns about potential toxicity [37]. Furthermore, the use of GC-delivering nanoplatfoms alone also poses challenges related to chronic rejection and long-term outcomes [38]. To address these challenges, we believe that a combined therapeutic strategy incorporating GC-delivering nanoplatfoms with other immunosuppressive drugs, such as calcineurin inhibitors and mycophenolate mofetil, could effectively reduce the overall dosage of each drug while maintaining or enhancing the desired immunosuppressive outcomes in clinical practice.

## Conclusions

In conclusion, our study highlights the promising therapeutic potential of a novel nanoplatfom, dNCPs@MM, composed of dexamethasone–Fe<sup>3+</sup> coordination polymers encapsulated within an outer macrophage membrane. In this study, dNCPs@MM demonstrated outstanding efficacy in suppressing acute rejection at

a low dosage and treating established rejection at a high dosage. To the best of our knowledge, this study is the first demonstration of utilizing membrane-coated nanoparticles for the treatment of acute rejection in solid organ transplantation. Furthermore, it is anticipated that this research will lay the groundwork for future investigations focused on membrane-coating strategies to address rejections in allografts and xenografts.

## Supplementary Information

The online version contains supplementary material available at <https://doi.org/10.1186/s12951-025-03226-z>.

Supplementary Material 1

## Acknowledgements

Not applicable.

## Author contributions

HB, SS and JY wrote the main manuscript text and prepared figures. HB and HL performed most experiments. SS and HL were responsible for data acquisition, analysis. XZ, YW and JY provided advice for the design of the study and revised the manuscript. DS helped in data analysis. FR, YW and JY were responsible for the conception, design and supervision of the study. All authors read and approved the final manuscript.

## Funding

This work was supported by the Fundamental Research Funds for the Central Universities (YG2023QNA04, YG2022QN027), and Shanghai Municipal Health Commission Clinical Research Project (20214Y0521).

## Data availability

All data generated or analysed during this study are available from the corresponding author on reasonable request.

## Declarations

### Ethics approval and consent to participate

All animal experiments were performed in accordance with the guidelines of the National Institute of Health for the Care and Use of Laboratory Animals and approved by the Committee on Ethics of Medicine of Naval Medical University (No. 202403006).

### Consent for publication

All the authors agree to the publication of the article.

### Competing interests

The authors declare no competing interests.

### Author details

<sup>1</sup>Department of Organ Transplantation, Shanghai Changzheng Hospital, Naval Medical University, Shanghai 200003, China

<sup>2</sup>Department of General Surgery, School of Medicine, Ruijin Hospital, Shanghai Jiao Tong University, Shanghai 200025, China

<sup>3</sup>School of Chemistry and Chemical Engineering, Shanghai Jiao Tong University, Shanghai 200240, China

Received: 7 December 2024 / Accepted: 11 February 2025

Published online: 07 April 2025

## References

- Nast CC. Polyomavirus nephropathy: diagnosis, histologic features, and differentiation from acute rejection. *Clin Transplant Res.* 2024 Apr 23.

2. Özçay N. Acute rejection pattern of an outbred strain combination on mouse-to-rat Heterotopic Heart Xenotransplantation. *Transpl Proc.* 2017;49(9):2215–8.
3. Ntobe-Bunkete B, Lemaitre F. Therapeutic drug monitoring in kidney and liver transplantation: current advances and future directions. *Expert Rev Clin Pharmacol* 2024 May-Jun;17(5–6):505–14.
4. Galati A, Brown ES, Bove R, Vaidya A, Gelfand J. Glucocorticoids for therapeutic immunosuppression: clinical pearls for the practicing neurologist. *J Neurol Sci.* 2021;430:120004.
5. Koning ACAM, Satoer DD, Vinkers CH, Zamanipoor Najafabadi AH, Biermasz NR, Nandoe Tewarie RDS, Moojen WA, van Rossum EFC, Dirven CMF, Pereira AM, van Furth WR, Meijer OC. The DEXA-CORT trial: study protocol of a randomised placebo-controlled trial of hydrocortisone in patients with brain tumour on the prevention of neuropsychiatric adverse effects caused by perioperative dexamethasone. *BMJ Open.* 2021;11(12):e054405.
6. Cheah JTL, Robson JC, Black RJ, Goodman SM, Lester S, Mackie SL, Hill CL. The patient's perspective of the adverse effects of glucocorticoid use: a systematic review of quantitative and qualitative studies. From an OMERACT working group. *Semin Arthritis Rheum.* 2020;50(5):996–1005.
7. Ning X, Zhu X, Wang Y, Yang J. Recent advances in carbon monoxide-releasing nanomaterials. *Bioact Mater.* 2024;37:30–50.
8. Sun D, Feng X, Zhu X, Wang Y, Yang J. Anticancer agents based on metal organic cages. *Coord Chem Rev.* 2024;500:215546.
9. Sun D, Deng Y, Dong J, Zhu X, Yang J, Wang Y. Heterometallic organic cages as cascade antioxidant nanozymes to alleviate renal ischemia-reperfusion injury. *Chem Eng J.* 2024;497:154648.
10. Yin P, Sun D, Deng Y, Zhu X, Wang Y, Yang J. Metal-organic cage as a theranostic nanoplatform for magnetic resonance imaging guided chemodynamic therapy. *Theranostics.* 2024;14:4861–73.
11. Ngobil TA, Daniele MA. Nanoparticles and direct immunosuppression. *Exp Biol Med (Maywood).* 2016;241(10):1064–73.
12. Yadav P, Rana K, Nardini V, Khan A, Pani T, Kar A, Jain D, Chakraborty R, Singh R, Jha SK, Mehta D, Sharma H, Sharma RD, Deo SVS, Sengupta S, Patil VS, Faccioli LH, Dasgupta U, Bajaj A. Engineered nanomicelles inhibit the tumour progression via abrogating the prostaglandin-mediated immunosuppression. *J Control Release.* 2024;368:548–65.
13. Cedrone E, Schuster M, Preyer R, Dobrovolskaia MA. Understanding the role of scavenger receptor A1 in nanoparticle uptake by Murine Macrophages. *Methods Mol Biol.* 2024;2789:293–8.
14. Yang J, Chen J, Young JS, Wang Q, Yin D, Sciammas R, Chong AS. Tracing Donor-MHC class II reactive B cells in mouse Cardiac Transplantation: delayed CTLA4-Ig treatment prevents memory alloreactive B-Cell generation. *Transplantation.* 2016;100(8):1683–91.
15. Khiew SH, Yang J, Young JS, Chen J, Wang Q, Yin D, Vu V, Miller ML, Sciammas R, Alegre ML, Chong AS. CTLA4-Ig in combination with FTY720 promotes allograft survival in sensitized recipients. *JCI Insight.* 2017;2(9):e92033.
16. Khiew SH, Jain D, Chen J, Yang J, Yin D, Young JS, Dent A, Sciammas R, Alegre ML, Chong AS. Transplantation tolerance modifies donor-specific B cell fate to suppress de novo alloreactive B cells. *J Clin Invest.* 2020;130(7):3453–66.
17. Polderman JAW, Farhang-Razi V, van Dieren S, Kranke P, DeVries JH, Hollmann MW, Preckel B, Hermanides J. Adverse side-effects of dexamethasone in surgical patients - an abridged Cochrane systematic review. *Anaesthesia.* 2019;74(7):929–39.
18. Bartling T, Oedingen C, Schrem H, Kohlmann T, Krauth C. As a surgeon, I am obliged to every single patient': evaluation of focus group discussions with transplantation physicians on the allocation of donor organs. *Curr Opin Organ Transpl.* 2021;26(5):459–67.
19. Anand RP, Layer JV, Heja D, Hirose T, Lassiter G, Firl DJ, Paragas VB, Akkad A, Chhangawala S, Colvin RB, Ernst RJ, Esch N, Getchell K, Griffin AK, Guo X, Hall KC, Hamilton P, Kalekar LA, Kan Y, Karadagi A, Li F, Low SC, Matheson R, Nehring C, Otsuka R, Pandelakis M, Policastro RA, Pols R, Queiroz L, Rosales IA, Serkin WT, Stiede K, Tomosugi T, Xue Y, Zentner GE, Angeles-Albores D, Chris Chao J, Crabtree JN, Harken S, Hinkle N, Lemos T, Li M, Pantano L, Stevens D, Subedar OD, Tan X, Yin S, Anwar IJ, Aufhauser D, Capuano S, Kaufman DB, Knechtle SJ, Kwun J, Shanmuganayagam D, Markmann JF, Church GM, Curtis M, Kawai T, Youd ME, Qin W. Design and testing of a humanized porcine donor for xenotransplantation. *Nature.* 2023;622(7982):393–401.
20. Pan W, Zhang W, Zheng B, Camellato BR, Stern J, Lin Z, Khodadadi-Jamayran A, Kim J, Sommer P, Khalil K, Weldon E, Bai J, Zhu Y, Meyn P, Heguy A, Mangiola M, Griesemer A, Keating BJ, Montgomery RA, Xia B, Boeke JD. Cellular dynamics in pig-to-human kidney xenotransplantation. *Med.* 2024 May 19;S2666-6340(24)00207-1.
21. Wu Y, Wan S, Yang S, Hu H, Zhang C, Lai J, Zhou J, Chen W, Tang X, Luo J, Zhou X, Yu L, Wang L, Wu A, Fan Q, Wu J. Macrophage cell membrane-based nanoparticles: a new promising biomimetic platform for targeted delivery and treatment. *J Nanobiotechnol.* 2022;20(1):542.
22. Lopes J, Lopes D, Pereira-Silva M, Peixoto D, Veiga F, Hamblin MR, Conde J, Corbo C, Zare EN, Ashrafzadeh M, Tay FR, Chen C, Donnelly RF, Wang X, Makvandi P, Paiva-Santos AC. Macrophage cell membrane-cloaked nanoplat-forms for Biomedical Applications. *Small Methods.* 2022;6(8):e2200289.
23. Ou Z, Zhong H, Zhang L, Deng M, Zhang W, Wang J, Feng H, Gong J, Miao C, Yi Z. Macrophage membrane-coated nanoparticles alleviate hepatic ischemia-reperfusion Injury caused by Orthotopic Liver transplantation by neutralizing endotoxin. *Int J Nanomed.* 2020;15:4125–38.
24. Qin X, Zhu L, Zhong Y, Wang Y, Luo X, Li J, Yan F, Wu G, Qiu J, Wang G, Qu K, Zhang K, Wu W. Universal cell membrane camouflaged nano-prodrugs with right-side-out orientation adapting for positive pathological vascular remodeling in atherosclerosis. *Chem Sci.* 2024;15(20):7524–44.
25. Jia Y, Zhang L, Xu J, Xiang L. Recent advances in cell membrane camouflaged nanotherapeutics for the treatment of bacterial infection. *Biomed Mater.* 2024;19(4).
26. Dashti-Khavidaki S, Saidi R, Lu H. Current status of glucocorticoid usage in solid organ transplantation. *World J Transpl.* 2021;11(11):443–65.
27. Redondo JM, Fresno M, López-Rivas A. Inhibition of interleukin 2-induced proliferation of cloned murine T cells by glucocorticoids. Possible involvement of an inhibitory protein. *Eur J Immunol.* 1988;18(10):1555–9.
28. Shen C, Xue X, Zhang X, Wu L, Duan X, Su C. Dexamethasone reduces auto-antibody levels in MRL/lpr mice by inhibiting Tfh cell responses. *J Cell Mol Med.* 2021;25(17):8329–37.
29. Pazdrak K, Moon Y, Straub C, Stafford S, Kurosky A. Eosinophil resistance to glucocorticoid-induced apoptosis is mediated by the transcription factor NFIL3. *Apoptosis.* 2016;21(4):421–31.
30. Borin C, Pieters T, Serafin V, Ntziachristos P. Emerging epigenetic and Post-translational Mechanisms Controlling Resistance to glucocorticoids in Acute Lymphoblastic Leukemia. *Hemisphere.* 2023;7(7):e916.
31. Young JS, Khiew SH, Yang J, Vannier A, Yin D, Sciammas R, Alegre ML, Chong AS. Successful treatment of T cell-mediated Acute rejection with delayed CTLA4-Ig in mice. *Front Immunol.* 2017;8:1169.
32. Nakao T, Nakamura T, Masuda K, Matsuyama T, Ushigome H, Ashihara E, Yoshimura N. Dexamethasone Prolongs Cardiac Allograft Survival in a Murine Model Through Myeloid-derived Suppressor Cells. *Transplant Proc.* 2018 Jan-Feb;50(1):299–304.
33. Zhao Y, Shen XF, Cao K, Ding J, Kang X, Guan WX, Ding YT, Liu BR, Du JF. Dexamethasone-Induced myeloid-derived suppressor cells prolong Allo Cardiac Graft Survival through iNOS- and glucocorticoid receptor-dependent mechanism. *Front Immunol.* 2018;9:282.
34. van Vugt LK, van der Zwan M, Clahsen-van Groningen MC, van Agteren M, Hullegie-Peelen DM, De Winter BCM, Reinders MEJ, Miranda Afonso P, Hesselink DA. A decade of experience with Alemtuzumab Therapy for severe or glucocorticoid-resistant kidney transplant rejection. *Transpl Int.* 2023;36:11834.
35. Meng T, Zheng J, Chen M, Zhao Y, Sudarjat H, M R AA, Kulkarni V, Oh Y, Xia S, Ding Z, Han H, Anders N, Rudek MA, Chow W, Stark W, Ensign LM, Hanes J, Xu Q. Six-month effective treatment of corneal graft rejection. *Sci Adv.* 2023;9(12):eadf4608.
36. Kim SJ, Kim JY, Kim EJ, Lee H, Cho Y, Kim MS, Kim YS, Kim BS, Huh KH. The Immunomodulating effects of Thalidomide and Dexamethasone in a murine cardiac allograft transplantation model. *Yonsei Med J.* 2022;63(2):158–65.
37. Furuta S, Nakagomi D, Kobayashi Y, Hiraguri M, Sugiyama T, Amano K, Umibe T, Kono H, Kurasawa K, Kita Y, Matsumura R, Kaneko Y, Ninagawa K, Hiromura K, Kagami SI, Inaba Y, Hanaoka H, Ikeda K, Nakajima H. LoVAS collaborators. Effect of reduced-dose vs high-dose glucocorticoids added to Rituximab on Remission induction in ANCA-Associated Vasculitis: a Randomized Clinical Trial. *JAMA.* 2021;325(21):2178–87.
38. Lühder F, Reichardt HM. Novel Drug Delivery Systems Tailored for Improved Administration of Glucocorticoids. *Int J Mol Sci.* 2017;18(9):1836.

**Publisher's note**

Springer Nature remains neutral with regard to jurisdictional claims in published maps and institutional affiliations.